RSC Advances

PAPER

View Article Online
View Journal | View Issue

Cite this: *RSC Adv.*, 2025, **15**, 38454

From discarded to desired: valorization of Zn–C battery waste into crystalline ZnO nanoparticles with crystallographic insights and antibacterial efficacy

Mashrafi Bin Mobarak, *[a] Md Sohag Hossain, [a] Fariha Chowdhury, [b] Nourin Tarannum, [c] Monira Binte Mesbah, [d] Nazmul Islam Tanvir, [e] Umme Sarmeen Akhtar [a] and Samina Ahmed *[a]

This study presents a sustainable "waste-to-wealth" approach for synthesizing zinc oxide nanoparticles (ZnO NPs) from discarded Zn–C dry cell batteries. The recovered Zn shells of the batteries were processed *via* a wet chemical route and calcination that yielded phase-pure wurtzite ZnO with nanoscale crystallite size, as confirmed by XRD analysis. A comprehensive crystallographic analysis was carried out to estimate crystallite size by exploiting various methods where Halder–Wagner and size–strain plot methods showed best fit to the experimental data (35.10 nm size and $R^2 = 0.967$). Band structure analysis using XPS/UPS revealed valence and conduction band edges relative to the vacuum level at −11.89 eV and −7.15 eV respectively, while the optical studies showed a wide band gap of 4.74 eV. FESEM analysis revealed assorted morphologies with an average particle size of 146 ± 89 nm, while TEM showed a more resolved average primary particle size of 40 ± 27 nm, corroborating the XRD analysis. Functional group analysis by FTIR and Raman spectroscopy confirmed the characteristic Zn–O stretching and the E_2 (high) vibrational modes. The as prepared ZnO NPs displayed antibacterial activity against Gram-positive bacteria (*Bacillus subtilis* and *Staphylococcus aureus*). However, no significant activity was observed against the tested Gram-negative strains. This work demonstrates a facile route to transform hazardous battery waste into functional ZnO NPs with promising structural and antibacterial properties.

Received 5th September 2025
Accepted 6th October 2025

DOI: 10.1039/d5ra06684k

rsc.li/rsc-advances

1 Introduction

The escalating global demand for portable electronic devices has led to a surge in the production and consumption of disposable batteries, with the global zinc–carbon (Zn–C) battery market valued at over USD 1.2 billion.[1,2] Among these, zinc–carbon dry cells are ubiquitous due to their low cost and wide availability.[3] However, their short lifespan results in a massive volume of hazardous waste. When improperly discarded in landfills, these batteries corrode and leak heavy metals like zinc and manganese, along with corrosive electrolytes, into the soil and groundwater. This contamination poses a significant threat to ecosystems and human health.[4,5] The release of zinc into soil and water systems can cause excessive accumulation of zinc which ultimately disrupts microbial communities, affects plant growth, and alters soil chemistry.[6] In aquatic ecosystems, elevated zinc concentrations are toxic to fish and other organisms due to bioaccumulation and interference with enzymatic processes.[7] For humans, chronic exposure to high zinc levels has been linked to gastrointestinal distress, immune system dysfunction, and interference with the metabolism of other essential trace elements such as copper.[8,9] Therefore, developing sustainable methods to manage battery waste is a critical environmental imperative. Although zinc is not considered to be a scarce metal because of its abundance in Earth's crust and widespread use in industries, the challenge lies in its recovery from hazardous wastes. Instead of treating spent batteries as refuse, they can be viewed as a valuable secondary resource. The concept of waste valorization, or "waste-to-wealth," offers a promising pathway to mitigate pollution while creating value. Specifically, the zinc casings from waste Zn–C batteries can be recycled and upcycled

[a]*Institute of Glass and Ceramic Research and Testing (IGCRT), Bangladesh Council of Scientific and Industrial Research (BCSIR), Dhaka-1205, Bangladesh. E-mail: mashrafibinmobarak@gmail.com; shanta_samina@yahoo.com*
[b]*Biomedical and Toxicological Research Institute (BTRI), Bangladesh Council of Scientific and Industrial Research (BCSIR), Dhaka-1205, Bangladesh*
[c]*Institute of Technology Transfer and Innovation (ITTI), Bangladesh Council of Scientific and Industrial Research (BCSIR), Dhaka-1205, Bangladesh*
[d]*Pilot Plant and Process Development Centre (PP & PDC), Bangladesh Council of Scientific and Industrial Research (BCSIR), Dhaka-1205, Bangladesh*
[e]*BCSIR Dhaka Laboratories, Bangladesh Council of Scientific and Industrial Research (BCSIR), Dhaka-1205, Bangladesh*

into high-value nanomaterials, such as zinc oxide nanoparticles (ZnO NPs), creating a circular economy model that addresses both waste management and resource scarcity.[4,10]

Nanotechnology, the manipulation of matter on an atomic and molecular scale, has revolutionized numerous scientific and industrial fields.[11] Nanoparticles (NPs), materials with dimensions typically between 1 and 100 nanometers, exhibit unique physical, chemical, and biological properties compared to their bulk counterparts due to their high surface-area-to-volume ratio and quantum effects. Among the various types of NPs, metal oxide nanoparticles have garnered immense interest.[12] Zinc oxide (ZnO) is a particularly important n-type semiconductor with a wide direct band gap (~3.37 eV) and large exciton binding energy.[13] Its properties, including high chemical stability, piezoelectricity, biocompatibility, and low toxicity, makes it a versatile material for a wide range of applications.[14] These include its use in sunscreens, gas sensors, photocatalysis for environmental remediation, and as a key component in electronic and optoelectronic devices. Furthermore, the potent antimicrobial properties of ZnO NPs have established them as a promising alternative to traditional antibiotics in biomedical and agricultural sectors.[15,16]

This study is motivated by the dual goals of environmental remediation and the sustainable synthesis of functional materials. We present a facile and cost-effective method to synthesize ZnO NPs by utilizing zinc recovered from the discarded shells of commercial Zn–C dry cell batteries. The novelty of this work lies on its waste-valorizing approach as well as the comprehensive structural characterization of the resulting nanomaterial. We employed an extensive array of ten different analytical models, including the Scherrer, Williamson–Hall (W–H), Halder–Wagner (H–W), and Size–Strain Plot (SSP) methods, to meticulously analyze the X-Ray Diffraction (XRD) data. This in-depth crystallographic investigation provides a precise understanding of key microstructural parameters like crystallite size, lattice strain, and dislocation density, which are crucial for determining the material's performance. Furthermore, given the growing concern over antibiotic resistance, we investigated the antibacterial activity of the synthesized ZnO NPs against both Gram-positive and Gram-negative pathogenic bacteria, aiming to validate their potential for biomedical applications.

2 Materials and methods

2.1. Materials

Waste dry cells were collected locally (spent household) and used as the primary source for Zn. Analytical-grade nitric acid (HNO_3, CAS: 7697-37-2) and sodium hydroxide (NaOH, CAS: 1310-73-2) were purchased from Merck KGaA, Germany, and used without further purification. Ethanol (CAS: 64-17-5) with a purity of ≥99.5% was obtained from Sigma-Aldrich. Deionized (DI) water was used throughout all synthesis and washing procedures.

2.2. Synthesis of ZnO from waste dry cell battery

First, a total of 6 AA type Zn–C waste dry cell batteries were collected and manually disassembled with pliers to isolate the Zn-containing components. The outer metallic casing (inside the steel cover and plastic separator), which serves as the anode in most Zn–C commercial dry cells, was identified as the primary source of Zn. These Zn shells were carefully separated from the inner components such as carbon rods, manganese dioxide paste, and insulating materials. A typical zinc shell of a Zn–C battery contains 98.0% of Zn as a new anode and 96.2% of Zn as spent anode.[17] The retrieved Zn shells were thoroughly washed and scrubbed with tap water followed by acetone and DI water to remove adhering electrolytes, manganese residues, and carbon particles. To ensure complete surface cleaning, the shells were then rinsed with ethanol and dried at room temperature for 24 hours prior to further chemical processing.

Cleaned Zn shells (3 g) were cut into small pieces to increase surface area for the reaction and slowly added to 50 mL of 10% (v/v, 1.45 M) HNO_3 solution under constant stirring at room temperature. This led to the formation of a clear zinc nitrate solution [$Zn(NO_3)_2$] through the following reaction.

$$Zn\ (s) + 2HNO_3\ (aq) \rightarrow Zn(NO_3)_2\ (aq) + H_2\ (g)\uparrow$$

To this solution, 1 M NaOH was added dropwise with constant stirring until the pH reached approximately 9.0. A white gelatinous precipitate of zinc hydroxide ($Zn(OH)_2$) resulted from this addition. The mixture was then stirred for an additional 10 minutes to ensure complete precipitation. The precipitate was then separated from the solution by vacuum filtration, dispersed in DI water with constant stirring for a thorough wash and filtered again. This was done several times that allowed us to remove residual nitrate and sodium ions. This is particularly a crucial step of the synthesis process and skipping this may result in the presence of $NaNO_3$ in the final product. The washed and filtered $Zn(OH)_2$ was dried for 12 hours in an oven at 80 °C, followed by grinding into a fine powder using a mortar–pestle. The amount of obtained $Zn(OH)_2$ powder was 3.95 g which was the precursor stock for ZnO and stored in an air tight condition for future use. Finally, 1 g of the $Zn(OH)_2$ powder was transferred to a ceramic crucible and calcined in a muffle furnace at 350 °C for 3 hours to obtain ZnO NPs *via* thermal decomposition. After cooling, 0.80 g of white ZnO NPs powder was obtained. Theoretically, 1 g of $Zn(OH)_2$ results in 0.82 g of ZnO and based on this approximation, our yield% was more than 97%. Synthesis scheme of ZnO NPs by utilizing waste Zn shells of Zn–C batteries is illustrated in Fig. 1.

2.3. Techniques of characterization

The synthesized ZnO NPs were examined for their structural and morphological characteristics using a range of analytical techniques. XRD patterns were obtained with Panalytical Empyrean EMP3 XRD instrument equipped with Cu-Kα radiation ($\lambda = 1.5406$ Å) and operated at 40 mA, 45 kV. X'pert HighScore Plus software was used for analyzing the XRD data. The presence of functional groups and bonding features was assessed through FTIR and Raman spectroscopy. FTIR spectra were recorded on a Shimadzu IR Prestige21 spectrometer fitted with an ATR accessory, covering the 4000–400 cm^{-1} region,

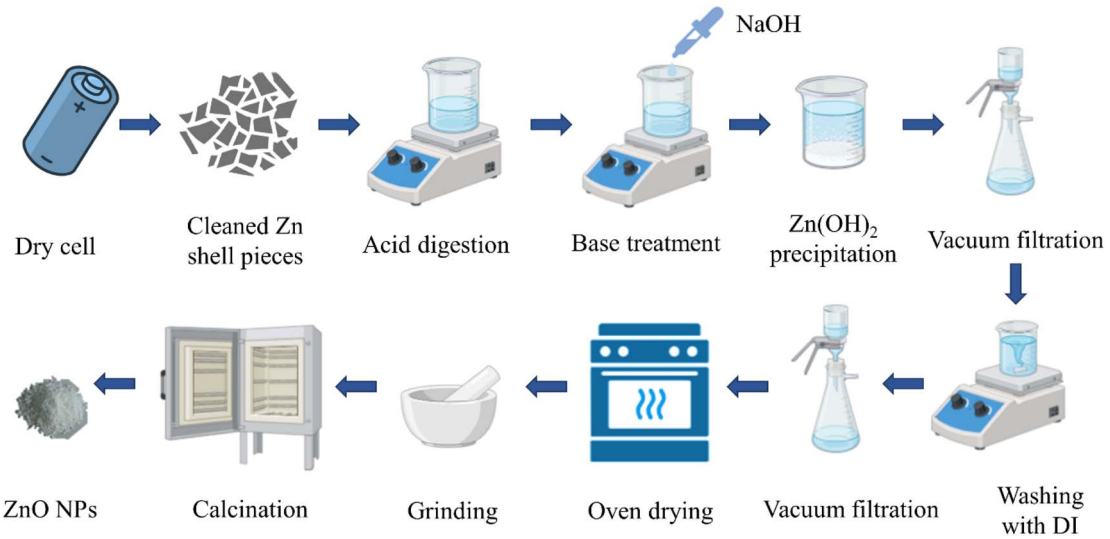

Fig. 1 Synthesis scheme of ZnO NPs by utilizing Zn–C battery waste.

averaging 30 scans at a resolution of 4 cm^{-1}. Raman spectra were acquired using a Horiba MacroRam spectrometer with a 785 nm excitation laser, calibrated against the standard silicon band near 520 cm^{-1}. Surface morphology was investigated using field emission scanning electron microscopy (FESEM, JEOL JSM-7610F) and transmission electron microscopy (TEM, Talos F200X G2). For FESEM analysis, samples were coated with platinum, while TEM specimens were prepared by drop-casting ethanol-dispersed nano-powders onto carbon-coated copper grids. Elemental composition was analyzed by EDS attached to the FESEM, employing a 1 nA probe current and ZAF correction for quantitative evaluation. The optical properties were further characterized by UV-visible spectroscopy using a Hitachi U-2910 spectrophotometer. Surface chemistry analysis was carried out by Thermo Scientific K-Alpha XPS instrument.

2.4. Protocol for antibacterial activity study

The *in vitro* antibacterial activity of ZnO NPs was determined by agar-well diffusion method.[18] The activity was tested against two Gram-positive (*Bacillus subtilis* ATCC 6633 and *Staphylococcus aureus* ATCC 29737) and two Gram-negative (*Escherichia coli* ATCC 11229 and *Pseudomonas aeruginosa* ATCC 10145) bacteria.[19] Briefly, 20–25 mL of sterile Mueller Hinton Agar (MHA) was poured in 90 mm Petri plates and subjected to solidification under sterile condition. Subsequently, 50 μL of freshly cultured bacterial suspensions ($\sim 10^5$ Colony Forming Unit (CFU) per 100 mL, $OD_{600} = 0.05$) were spread on the agar surface with sterile cotton swab. Afterward, 6 mm wells were prepared with sterile cork-borer on the pre-inoculated agar surface and 100 μL of 0.1–0.5 mg mL^{-1} solutions were placed on the wells. Tetracycline disc was used as positive control for all except *Pseudomonas aeruginosa* for which ciprofloxacin disc was used and the negative control was the solvent (dimethyl sulfoxide (DMSO)). The plates were incubated for 24 h at 37 °C and the zone of inhibition around each well was evaluated with a millimeter scale. The experiments were conducted three times ($n = 3$) independently and the average value of these trials and their standard errors were computed and represented as mean ± standard deviation (SD).

3 Results and discussion

3.1. X-ray powder diffraction study

3.1.1. Phase identification. The XRD pattern of the synthesized ZnO NPs (Fig. 2a) confirms the formation of a highly crystalline hexagonal wurtzite structure, which is the most thermodynamically stable phase of ZnO under ambient conditions.[20] The diffraction peaks observed in the XRD pattern match precisely with the ICDD (International Centre for Diffraction Data) card no. 01-080-0074, which depicts the successful synthesis of phase-pure ZnO.[21] The sharpest Bragg peak was observed at a 2θ value of 36.20°, corresponding to the (101) crystal plane. This peak was accompanied by two other sharp peaks at 2θ values of 31.76° (100) and 34.42° (002), respectively.[22] These planes are characteristic of the hexagonal wurtzite crystal system with space group $P6_3mc$ (186).[23] Among them, the (101) plane shows the highest intensity, suggesting that the crystallites exhibit preferential growth along this plane. This is consistent with previously reported studies on ZnO NPs synthesized *via* wet chemical, sol–gel, hydrothermal or even biosynthesis routes, where the (101) plane is often the most prominent due to its lower surface energy.[24–27] The sharpness and high intensity of the peaks reflect good crystallinity of the ZnO NPs, indicating that the calcination temperature of 350 °C was sufficient to transform the $Zn(OH)_2$ completely into crystalline ZnO while minimizing sintering and subsequent particle growth. Moreover, the absence of additional peaks confirms the phase purity of the sample, with no detectable secondary phases or residual impurities such as $Zn(OH)_2$, $Zn(NO_3)_2$, or $NaNO_3$ (from the used NaOH), which supports the effectiveness of the washing and calcination steps. All the peaks detected and their

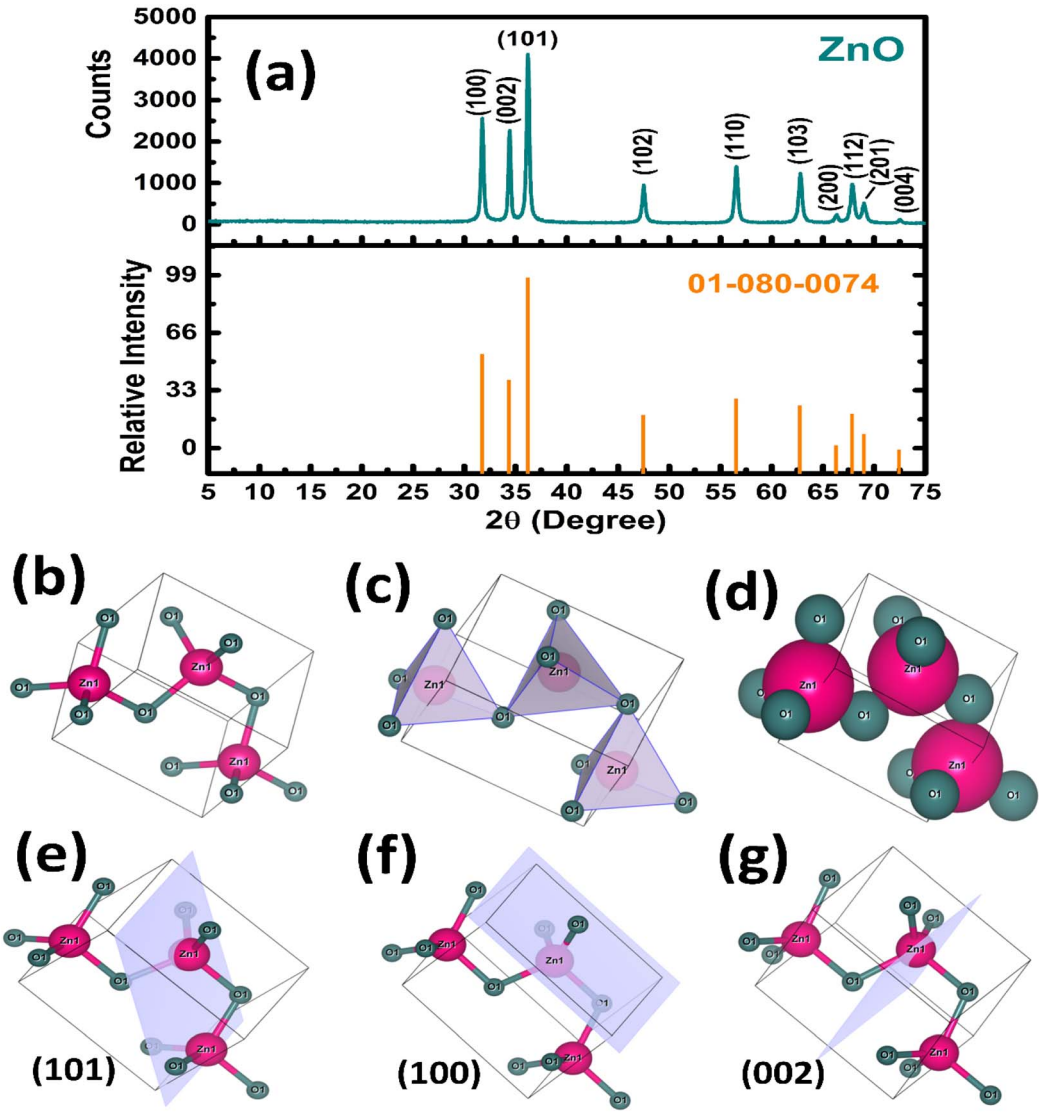

Fig. 2 (a) XRD pattern of the synthesized ZnO NPs utilizing Zn–C battery waste; (b) ball-and-stick (c) polyhedral, and (d) space-filling crystal structure; three major crystal planes (e) 101 (f) 100 and (g) 002 of ZnO as observed in the XRD pattern. CIF file of ZnO was taken from crystallography open database which was then imported to VESTA 3.90.1a software. Lattice parameters were also inserted to customize the structure in accordance with our calculated values from Table 2.

corresponding XRD-based information are presented in Table 1. Crystal structure of the synthesized ZnO is illustrated in Fig. 2b–g. Rietveld refinement of the XRD data was performed (Profex version 5.5.1) to confirm the phase purity and crystal structure of the synthesized ZnO NPs. The refinement yielded a good fit with a weighted profile *R*-factor (R_{wp}) of 12.88%, an

Table 1 XRD based crystallographic parameters of the synthesized ZnO NPs

Crystal plane	2θ degree	θ degree	Cos θ radian	*d*-spacing (Å)	FWHM (β) degree	1/FWHM ($1/\beta$) radian	Crystallite size, $D = \frac{k\lambda}{\beta \cos\theta}$ (nm)	Average crystallite size (nm)
(100)	31.76	15.88	0.9618	2.82	0.2283	250.9803	36.18	35.29
(002)	34.42	17.21	0.9552	2.61	0.1998	286.8346	41.64	
(101)	**36.20**	**18.10**	**0.9505**	**2.48**	**0.2568**	**223.0936**	**32.54**	
(102)	47.51	23.76	0.9153	1.91	0.3139	182.5311	27.65	
(110)	56.55	28.28	0.8807	1.63	0.25682	223.0936	35.12	
(103)	62.77	31.38	0.8537	1.48	0.25682	223.0936	36.23	
(200)	66.33	33.16	0.8371	1.41	0.34243	167.3202	27.71	
(112)	67.88	33.94	0.8296	1.38	0.22829	250.9803	41.95	
(201)	69.00	34.50	0.8241	1.36	0.31389	182.5311	30.71	
(004)	72.51	36.26	0.8064	1.30	0.22829	250.9803	43.16	

expected R-factor (R_{exp}) of 8.69%, and a goodness-of-fit (χ^2) of 2.1968. The refined XRD pattern is presented in Fig. 3a.

3.1.2. Crystallographic analysis and microstructural parameters. The XRD data was utilized for calculating the crystallographic and microstructural parameters of the synthesized ZnO NPs. As confirmed by the XRD analysis, the synthesized ZnO was hexagonal crystal structured and hence, following equations (eqn (1) to (8)) were employed for estimating the lattice parameter, volume and density of unit cell, micro-strain, crystallite size based on Scherrer's formula, dislocation density and Zn–O bond length.

$$\text{Lattice parameter of hexagonal structure, } \frac{1}{d^2} = \frac{4}{3}\left(\frac{h^2+hk+k^2}{a^2}\right)+\frac{l^2}{c^2} \quad (1)$$

$$\text{Volume of unit cell, } V = \frac{\sqrt{3}}{2}a^2c \quad (2)$$

$$\text{Density of unit cell, } \rho = \frac{nA}{N_A V_c} \quad (3)$$

$$\text{Micro-strain, } \varepsilon = \frac{\beta}{4\tan\theta} \quad (4)$$

$$\text{Crystallite size, } D = \frac{k\lambda}{\beta\cos\theta} \quad (5)$$

$$\text{Dislocation density, } \delta = \frac{1}{D^2} \quad (6)$$

$$\text{Zn} - \text{O bond length, } L = \sqrt{\left(\frac{a^2}{3}+\left(\frac{1}{2}-u\right)^2 c^2\right)} \quad (7)$$

In the above equations, a, b, c = dimensions of unit cell; h, k, l = Miller indices used for crystal plane representation; d = inter-planar distance; β = angle between a and c; V = volume of hexagonal crystal structure; ρ = density; n = number of atoms per unit cell (2 for ZnO NPs); A = atomic weight (81.38 g mol^{-1} for ZnO); N_A = Avogadro number (6.023 × 10^{23} mol^{-1}); V_C = volume of unit cell calculated from eqn (2); ε = micro-strain; β = full width half maxima (FWHM); θ = diffraction angle; D = crystallite size; K = form factor (0.9 for ceramic materials); λ = wavelength of the generated X-ray (0.154060 nm for this instrument); δ = dislocation density which was calculated

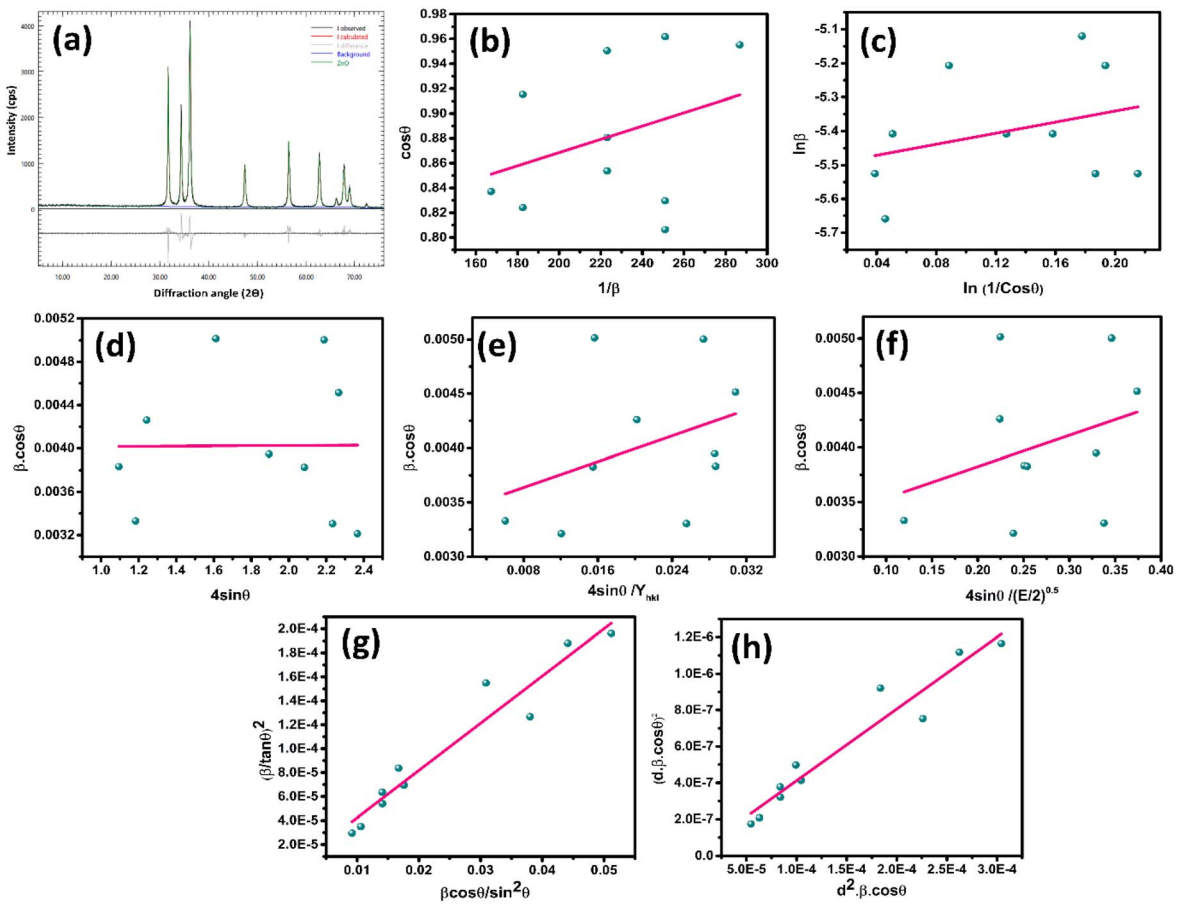

Fig. 3 (a) Rietveld refinement of XRD pattern of synthesized ZnO NPs; crystallite size analysis by linear fitting of the plots of (b) linear straight-line method (LSLM), (c) Monshi–Scherrer method (M–SM), Williamson–Hall method (W–HM): (d) Uniform Deformation Method (UDM), (e) Uniform Stress Deformation Method (USDM), (f) Uniform Deformation Energy Density Method (UDEDM), (g) Halder–Wagner Method (H–WM), and (h) Size–Strain Plot Method (SSPM).

utilizing crystallite size from the Scherrer's formula; and u = positional parameter in the wurtzite structure which is calculated by the following formula.[28]

$$\text{Positional parameter, } u = \frac{a^2}{3c^2} + 0.25 \quad (8)$$

Within crystalline materials, relative intensity serves as a quantitative measure for assessing the diffraction intensity associated with specific crystallographic planes. It is typically determined by calculating the ratio of the intensity of a designated plane to the aggregate intensity of other prominent planes within the diffraction pattern. Additionally, the phenomenon of preference growth provides insight into the propensity of crystallites to exhibit alignment along particular crystallographic planes during the process of material formation.[29,30] The following equations represent the formula for calculating relative intensity and preference growth of the synthesized ZnO NPs, respectively.

$$\text{Relative intensity, } \mathrm{RI}_{\mathrm{ZnO}} = \frac{I_{(101)}}{I_{(100)} + I_{(002)} + I_{(110)}} \quad (9)$$

$$\text{Preference growth} = \frac{\mathrm{RI}_{\mathrm{sample}} - \mathrm{RI}_{\mathrm{standard}}}{\mathrm{RI}_{\mathrm{standard}}} \quad (10)$$

In the above equations, $I_{(101)}$, $I_{(100)}$, $I_{(002)}$ and $I_{(110)}$ represent intensities of the top four crystal planes in the decreasing order. The RI calculated in such manner is then used for calculating the preference growth (eqn (10)), where RI of the standard is taken from the ICDD card #01-080-0074.

The quantitative representation of the degree of order, known as crystallinity index (CI), can be calculated based on the XRD data for our synthesized ZnO NPs. Following equations represents the expression for crystallinity index calculation.

$$\text{Crystallinity index, CI} = X_{\mathrm{C}} = \left(\frac{K_{\mathrm{a}}}{\beta_{(101)}}\right)^3 \quad (11)$$

$$\text{Crystallinity index, CI} = \mathrm{CI}_{\mathrm{XRD}} = \sum \frac{H_{(100)} + H_{(002)} + H_{(110)}}{H_{(101)}} \quad (12)$$

In the mathematical expressions presented above, K_{a} = constant (taken as 0.24); $\beta_{(101)}$ = FWHM of the (101) plane which is the most intense peak. $H_{(100)}$, $H_{(002)}$, $H_{(110)}$, and $H_{(101)}$ are the heights of the peaks at the (100), (002), (110), and (101) planes, respectively.

An idea of specific surface area (SSA) of the synthesized ZnO NPs can be obtained from the following equation, which assumes the particles to be spherical and non-porous. It also neglects particle shape irregularities, porosity, and agglomeration effects, making it an approximation rather than a precise measurement.[31,32]

$$\text{Specific surface area, SSA} = \frac{6}{\rho \times D} \quad (13)$$

Here, ρ is the density of unit cell of ZnO NPs as calculated using eqn (3) and D is the crystallite size calculated from eqn (5). SSA is expressed in $\mathrm{m^2\ g^{-1}}$ unit.

The texture coefficient (TC) of our synthesized ZnO NPs was also measured. This TC refers to the preferred orientation of crystallites in a polycrystalline material. It is calculated by comparing the relative intensity of a specific diffraction peak to standard reference data. It indicates which crystallographic planes are more prominently oriented in the sample.[33,34] The formula of TC is presented below.[35]

$$\mathrm{TC}_{(hkl)} = \frac{I_{\mathrm{sample}\ (hkl)} / I_{\mathrm{standard}\ (hkl)}}{\frac{1}{N}\sum_{n=1}^{N}\left(I_{\mathrm{sample}\ (hkl)} / I_{\mathrm{standard}\ (hkl)}\right)} \quad (14)$$

In this mathematical expression, $I_{\mathrm{sample}\ (hkl)}$ and $I_{\mathrm{standard}\ (hkl)}$ are the measured intensity of the (hkl) reflection of ZnO sample and standard intensity of the (hkl) reflection from the reference (ICDD card #01-080-0074), N = total number of considered reflections.

The crystallographic parameters obtained from the above discussed expressions are tabulated in Table 2, except for the texture coefficient values which is shown separately in Table 3.

As shown in the presented data Table 2, the calculated lattice parameters are closely matching the ICDD reference data which indicates high phase purity and successful synthesis of ZnO without significant lattice distortion. Values of crystallinity index indicate moderately high crystallinity, which is

Table 2 Microstructural parameters of the Zn–C waste battery derived ZnO NPs

Parameters	ZnO NPs	ICDD file #01-080-0074
Unit cell dimensions (Å) of the hexagonal crystal structure	$a = b = 3.2537$ $c = 5.2107$	$a = b = 3.2535$ $c = 5.2151$
Volume of unit cell, V (Å^3)	47.77	47.81
Density of unit cell, ρ (g cm^{-3})	5.66	5.65
Micro-strain, ε	0.19	—
Crystallite size based on Scherrer equation, D (nm)	32.54	—
Dislocation density, δ (nm^{-2}) $\times 10^{-3}$	0.94	—
Zn–O bond length, L (Å)	1.98	—
Relative intensity, $\mathrm{RI}_{\mathrm{ZnO}}$	0.68	5.44
Preference growth	−0.88	—
Crystallinity index (CI = X_{c})	0.82	—
Crystallinity index (CI = $\mathrm{CI}_{\mathrm{XRD}}$)	1.48	—
Specific surface area, SSA (m^2 g^{-1})	32.58	—

Table 3 Texture coefficient calculations of the synthesized ZnO NPs

Crystal plane	$I_{sample\ (hkl)}$	$I_{standard\ (hkl)}$	$I_{sample\ (hkl)}/I_{standard\ (hkl)}$	Average, $\frac{1}{N}\sum_{n=1}^{N}(I_{sample\ (hkl)}/I_{standard\ (hkl)})$	Texture coefficient (TC)	Orientation (TC > 1 preferred TC < 1 suppressed TC = 1 random)
(100)	2380	60.66	39.24	$\frac{321.06}{7} = 39.22$	1.00	Random
(002)	2096	53.44	39.22		1.00	Random
(101)	3923	100	39.23		1.00	Random
(102)	871	22.20	39.23		1.00	Random
(110)	1333	33.98	39.23		1.00	Random
(103)	1106	28.19	39.23		1.00	Random
(112)	877	22.36	39.22		1.00	Random

advantageous for maintaining structural integrity while providing adequate surface defects for reactivity. An interesting point of analysis arises when comparing the preference growth and TC values. The preference growth calculation yielded a value of −0.88, which typically suggests a suppressed crystal orientation. However, the more comprehensive TC analysis for all major diffraction planes resulted in TC values of approximately 1.0, indicating a random crystallite orientation. This apparent discrepancy can be attributed to the different methodologies. The preference growth formula is based on a limited set of four peaks and is highly sensitive to the RI standard value of the reference powder, which in this case is high (5.44). In contrast, the TC calculation normalizes the intensity ratios across seven different planes. Given that the $I_{sample}/I_{standard}$ ratio is consistently ∼39.2 across all planes, the TC analysis is considered more robust. Therefore, we conclude that the synthesized ZnO NPs possess a random crystallite orientation, and the negative preference growth value is an artifact of comparing our sample to a standard with a particularly strong texture along the (101) plane. Crystal structure of ZnO at different orientations and formats are illustrated in Fig. 2b–g.

3.1.3. Crystallite size estimation. The estimation of crystallite size from X-ray diffraction data is critical for understanding the nanoscale structure of materials. A variety of analytical approaches have been developed to estimate crystallite size. Each method has its own level of complexity and assumptions regarding the broadening of peak. The crystallite size of our synthesized ZnO NPs was estimated by ten different methods, out of which three were direct calculation methods (Scherrer method, the Scherrer equation average method, and the straight line passing through origin method) and the rest seven were linear fit-based methods (linear straight-line method, Monshi–Scherrer method, Halder–Wagner method, Williamson–Hall methods (including uniform deformation, uniform stress deformation, and uniform deformation energy density), and the size–strain plot method).

3.1.3.1. Scherrer method (SM). Scherrer method is a fundamental technique for estimating crystallite size from X-ray diffraction peak broadening. It assumes that instrumental broadening and strain effects are negligible and that all observed broadening is due to crystallite size. The method originated from Paul Scherrer's work in 1918.[36,37] The Scherrer equation has been presented in eqn (5). A major limitation of this method is that, it only accounts for size broadening and does not differentiate between size and strain effects. This leads to an underestimation of crystallite size if strain is present. It also requires careful subtraction of instrumental broadening and is most reliable for crystallite sizes below 100 nm. The estimated crystallite size of ZnO NPs through SM is presented in Table 1.

3.1.3.2. Scherrer equation average method (SEAM). This method involves the exploitation of Scherrer equation to multiple diffraction peaks and then averages the calculated crystallite sizes.[29] With such tactic, this method attempts to provide a more representative average crystallite size by considering different crystallographic directions. The principle is the same as the single Scherrer equation, but D is averaged over multiple peaks. Similar to Scherrer's method, it also doesn't account for strain broadening. Additionally, averaging multiple peaks can sometimes disguise variations in crystallite size anisotropy if present, or lead to misleading averages if some peaks are significantly affected by strain. Estimation of crystallite size by SEAM is presented in Table 1.

3.1.3.3. Linear straight-line method (LSLM). The linear straight-line method refers to the graphical approach where a linear relationship is built to separate size and strain contributions to peak broadening. This method plots certain functions of peak broadening against other variables to extract crystallite size and strain from the slope and intercept.[38] Typically, it involves plotting of $\cos\theta$ *versus* $1/\beta$ and the linear fitting results in the slope which is equal to $K\lambda/D$. The crystallite size can be inferred from this.

$$\cos\theta = \frac{K\lambda}{D} \times \frac{1}{\beta} \tag{15}$$

3.1.3.4. Straight line passing through origin method (SLPOM). The SLPOM method is a variant of LSLM where the linear fit is constrained to pass through the origin which simplifies the analysis under certain assumptions. According to this method, if all broadening were due to strain and uniform, a plot of $\cos\theta$ *versus* $1/\beta$ would pass through the origin. Conversely, if only size broadening were present, it would be a horizontal line. The values of $1/\beta$ are taken as x, and the values of $\cos\theta$ as y. This leads to an equation that determines the slope of the straight line passing through the origin.[39]

$$\text{Slope} = \frac{x_1y_1 + x_2y_2 + x_3y_3 + \ldots + x_ny_n}{{x_1}^2 + {x_2}^2 + {x_3}^2 + \ldots {x_n}^2} \tag{16}$$

Table 4 Extracted values of $1/\beta$ as x and values of $\cos\theta$ as y from LSLM for calculating the crystallite size of synthesized ZnO NP using SLPOM

Values of x	250.98	286.83	223.09	182.53	223.09	223.09	167.32	250.98	182.53	250.98
Values of y	0.9618	0.9552	0.9505	0.9153	0.8807	0.8537	0.8371	0.8296	0.8241	0.8064

The slope of this equation is equal to $K\lambda/D$. From this relationship, crystallite size can be estimated easily. The values of x and y are obtained from LSLM and is presented in Table 4.

3.1.3.5. Monshi–Scherrer method (M–SM). In 2012, Monshi *et al.* introduced a modification to the conventional Scherrer equation to improve the accuracy of nanocrystallite size determination.[40] The original Scherrer equation often shows a systematic increase in calculated nanocrystallite size as the interplanar spacing decreases and the diffraction angle increases, since the product of peak broadening and the cosine of the Bragg angle does not remain constant. To address this, Monshi *et al.* proposed a linearized form of the Scherrer equation as shown below.

$$\ln\beta = \ln\frac{k\lambda}{D} + \ln\frac{1}{\cos\theta} \tag{17}$$

This modified approach involves a linear plot of $\ln\beta$ against $\ln(1/\cos\theta)$ using data from multiple diffraction peaks. The intercept of the resulting linear fit corresponds to $\ln(K\lambda/D)$. Exponentiation of this intercept yields $K\lambda/D$, from which a more accurate value for the crystallite size can be determined. This method offers an advantage by reducing the overall error in crystallite size estimation compared to applying the Scherrer equation to individual peaks.

3.1.3.6. Williamson–Hall method (W–HM). The Scherrer equation primarily focuses on XRD peak broadening caused by crystallite size. However, it does not account for broadening due to microstrain within the crystal lattice. Microstrain can arise from various lattice imperfections which are common in nanocrystalline materials. To address the limitations of the Scherrer equation and simultaneously determine both crystallite size and intrinsic strain, the W–HM method is employed. This method acknowledges that the total physical broadening (β_{total}) of an XRD peak is a combination of broadening due to crystallite size (β_{size}) and broadening due to microstrain (β_{strain}).[39,41]

$$\beta_{\text{total}} = \beta_{\text{size}} + \beta_{\text{strain}} \tag{18}$$

The W–HM can be applied using different models, which assume various conditions for a material's deformation. These models include the Uniform Deformation Method (UDM), the Uniform Stress Deformation Method (USDM), and the Uniform Deformation Energy Density Method (UDEDM). Each of these methods provides a specific framework for analyzing the interplay between crystallite size and strain in diffraction peak broadening.

3.1.3.6.1. Uniform deformation method (UDM). The UDM, also known as the uniform strain method, is the simplest W–H method, assuming that the strain is uniform in all crystallographic directions. This implies that the strain contribution to broadening is isotropic. The mathematical expression of this method is as follows.

$$\beta\cos\theta = \frac{K\lambda}{D} + 4\varepsilon\sin\theta \tag{19}$$

A graph is created by plotting $\beta\cos\theta$ on the y-axis against $4\sin\theta$ on the x-axis. The resulting linear fitted plot provides valuable information where the y-intercept directly corresponds to the crystallite size, while the slope of the line represents the strain within the material.

3.1.3.6.2. Uniform stress deformation method (USDM). The USDM considers that the stress is uniform in all crystallographic directions which implies that the strain varies with the elastic moduli of the material in different directions. This also addresses the anisotropic nature of the materials elasticity. According to Hooke's law, strain (ε) is related to stress (σ) by, $\sigma = Y_{hkl} \times \varepsilon$, where Y_{hkl} is Young's modulus in the (hkl) direction. Young's modulus (E_{hkl}) can be calculated from the following equation based on the hexagonal ZnO structure.

$$Y_{hkl} = \frac{\left(h^2+k^2+l^2\right)^2}{S_{11}\left(h^4+k^4+h^2k^2\right) + (2S_{12}+S_{66})h^2k^2 + \left(2S_{13}+S_{44)}\right)\left(h^2+k^2\right)l^2 + S_{33}l^4} \tag{20}$$

Here, S_{11}, S_{12}, S_{13}, S_{33}, S_{44}, and S_{66} are referred to as elastic compliance whereas C_{11}, C_{12}, C_{13}, C_{33}, C_{44}, and C_{66} refer to as the elastic stiffness constants. These values are taken from the cited ref. 42. Putting the value of ε in eqn (19), the following equation can be obtained.

$$\beta\cos\theta = \frac{K\lambda}{D} + 4\sigma\frac{\sin\theta}{Y_{hkl}} \tag{21}$$

Linear fitting of $\beta\cos\theta$ *versus* $4\sin\theta/Y_{hkl}$ plot results in the intercept which is equal to $K\lambda/D$ and thus, crystallite size is calculated.

3.1.3.6.3. Uniform deformation energy density model (UDEDM). The UDEDM is utilized to investigate anisotropic energy within materials. This method incorporates the concept of lattice energy density (LED), which quantifies the amount of elastic energy stored per unit volume within the crystal lattice. In this model, it is assumed that the volumetric LED is directly related to a crystal's effective stiffness along different crystallographic directions. According to the principles of Hooke's law, LED can be determined from the microstrain (ε) and Young's modulus (Y_{hkl}) specific to a given crystallographic plane (hkl) using the following relationship.[39]

$$\mathrm{LED} = \varepsilon^2 \frac{Y_{hkl}}{2} \tag{22}$$

$$\text{or, } \varepsilon = \sigma\sqrt{\frac{2\mathrm{LED}}{Y_{hkl}}} \tag{23}$$

By substituting this expression for strain into the general Williamson–Hall equation (eqn (17)), the UDEDM leads to the following equation.

$$\beta\cos\theta = \frac{K\lambda}{D} + 4\sigma\sin\theta\sqrt{\frac{2\mathrm{LED}}{Y_{hkl}}} \tag{24}$$

The crystallite size can be calculated from the linear fitted plot of $\beta\cos\theta$ *versus* $4\sin\theta/(Y_{hkl}/2)^{0.5}$ where the size is equal to the intercept.

3.1.3.7. Halder–Wagner method (H–WM). The H–WM refines the analysis of XRD peak broadening by modeling the peak profiles as a Voigt function. This function is a convolution of two components: a Lorentzian function, which primarily accounts for crystallite size-induced broadening, and a Gaussian function, which primarily accounts for strain-induced broadening. This approach improves the accuracy of crystallite size estimation, especially in nanocrystalline materials, by assuming a symmetric Voigt profile for the broadened peaks. The H-WM thus offers a more precise alternative compared to simpler techniques like the Scherrer equation. The FWHM of a Voigt profile (β_{hkl}) is related to the FWHM of its Lorentzian (β_L) and Gaussian (β_G) components by the following equation.[43]

$${\beta_{hkl}}^2 = \beta_L \times \beta_{hkl} + {\beta_G}^2 \tag{25}$$

The H-WM specifically focuses on regions of the diffraction pattern where peak overlap is minimal and thus giving more weight to Bragg peaks at lower and mid-angles. The relationship between crystallite size and lattice strain in the H-WM is described by the following equation.

$$\left(\frac{\beta}{\tan\theta}\right)^2 = \frac{K\lambda}{D} \times \frac{\beta\cos\theta}{\sin^2\theta} + 16\varepsilon^2 \tag{26}$$

A linear plot of $(\beta/\tan\theta)^2$ *versus* $(\beta\cos\theta/\sin^2\theta)$ can be constructed where the slope is related to the crystallite size, and the intercept provides information about the microstrain. This method proves particularly useful for materials where both crystallite size and strain significantly contribute to peak broadening, requiring their accurate separation.

3.1.3.8. Size–strain plot method (SSPM). The SSPM offers an alternative approach for analyzing XRD peak broadening by simultaneously considering both crystallite size and strain effects in a single graphical representation. This method operates on the assumption that broadening due to crystallite size can be described by a Lorentzian function, while strain broadening follows a Gaussian distribution. Based on these assumptions, the relationship between peak broadening and diffraction angle can be expressed as the following equation.[44,45]

$$(d\beta\cos\theta)^2 = \frac{K\lambda}{D} \times \left(d^2\beta\cos\theta\right) + \frac{\varepsilon^2}{4} \tag{27}$$

A linear relationship is obtained by plotting $(d\beta\cos\theta)^2$ against $d^2\beta\cos\theta$, where d is the interplanar spacing. In this plot, the slope is related to the crystallite size, specifically being equal to $K\lambda/D$, while the intercept provides information about the strain.

Linear fitted plots of the models that are used in calculating the crystallite size are presented in Fig. 3b–h and the resulting crystallite size and corresponding dislocation density values are compiled in Table 5.

Most of the models, such as SM, SEAM, SLPOM, M–SM, H–WM, and SSPM, yielded crystallite sizes in the range of 32–36 nm, indicating a consistent nanoscale dimension. The W–HM analysis showed slight variations, with the UDM giving 34.6 nm, while USDM and UDEDM gave larger values of 40.8 nm and 42.7 nm, respectively. In contrast, the crystallite size obtained from the LSLM (259.47 nm) shows a significant deviation from the values calculated by other models. This discrepancy might be arising due to the poor regression coefficient (R^2 = 0.337) that reflects a weak linear fitting of the diffraction data. Such poor fitting likely arises from peak broadening contributions due to lattice strain and defects which are not effectively accommodated in this method. The consistency among most methods confirms that the synthesized ZnO NPs possess a nanoscale crystallite size (~30–40 nm), with low dislocation density, suggesting good crystallinity.

3.2. XPS surface chemistry analysis

The XPS analysis of the synthesized ZnO NPs provides detailed insights into the elemental composition, chemical states, and electronic structure of the material. Fig. 4a shows the survey scan that confirms the presence of Zn and O as the primary elements, along with a minor C signal attributed to surface contamination or adventitious carbon commonly observed in XPS measurements.[29] The prominent Zn peaks include Zn 2p, Zn 2s, Zn 3d, and Zn Auger peaks (Zn LM series), while the O 1s signal is also clearly visible.

The ultraviolet photoelectron spectroscopy (UPS) results (Fig. 4b–d) provide information on the energy levels relative to the vacuum level. From the UPS cut-off region, the secondary

Table 5 Calculated crystallite size and dislocation density of the synthesized ZnO NPs by different methods

Method		FS-ATB CS (nm)	R^2	δ (nm^{-2}) × 10^{-4}
Scherrer's method (SM)		32.54	—	9.44
Scherrer equation average method (SEAM)		35.29 ± 5.70	—	9.59
Linear straight-line method (LSLM)		259.47	0.337	0.15
Straight line passing the origin (SLPOM)		36.03	—	7.70
Monshi–Scherrer method (M–SM)		32.14	0.319	9.68
Williamson–Hall method (W–HM)	Uniform deformation method (UDM)	34.58	0.007	8.36
	Uniform stress deformation method (USDM)	40.78	0.377	6.01
	Uniform deformation energy density method (UDEDM)	42.66	0.333	5.49
Halder–Wagner method (H–WM)		35.10	**0.967**	8.12
Size–strain plot method (SSPM)		35.10	**0.967**	8.12

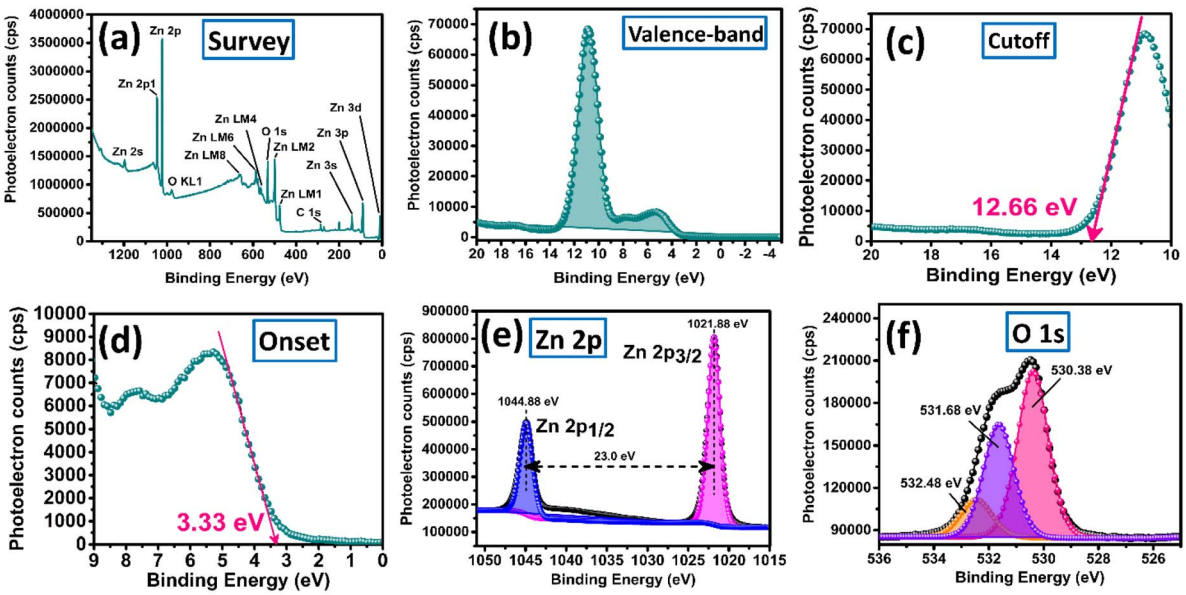

Fig. 4 XPS surface chemistry analysis of the synthesized ZnO NPs: (a) survey spectrum; ultraviolet photoelectron spectroscopy (UPS) showing the (b) valence band spectrum, (c) cut-off region, (d) onset region; (e) Zn 2p narrow scan spectrum, and (f) O 1s narrow scan spectrum.

electron cut-off energy (E_{cutoff}) was determined as 12.66 eV. Using the relation $E_f = E_{cutoff} - 21.22$ eV, the Fermi level (E_f) was calculated to be −8.56 eV on the vacuum energy scale. The valence band maximum (E_{VBM}) was further calculated from the onset energy using the relation $E_{VBM} = E_f - E_{onset}$, yielding an E_{VBM} of −11.89 eV (vacuum scale). The optical band gap (E_g) obtained from UV-visible spectroscopy and Tauc plot analysis was 4.74 eV. Accordingly, the conduction band minimum (E_{CBM}) was determined using $E_{CBM} = E_{VBM} + E_g$, resulting in −7.15 eV relative to the vacuum level. These negative values indicate that the energies are referenced to the vacuum level, with the conduction band lying closer to the vacuum than the valence band.[46]

The high-resolution Zn 2p spectrum (Fig. 4e) displays two distinct peaks at 1021.88 eV and 1044.88 eV, corresponding to Zn $2p_{3/2}$ and Zn $2p_{1/2}$, respectively. The observed spin–orbit splitting of 23.0 eV is consistent with reported values for Zn^{2+} in ZnO,[47] confirming the +2 oxidation state of zinc and the absence of metallic Zn or other zinc species. The sharpness of the peaks further indicates the well-defined chemical state of Zn in the NPs.

The deconvoluted O 1s spectrum (Fig. 4f) reveals three components located at 530.38 eV, 531.68 eV, and 532.48 eV. The peak at 530.38 eV is attributed to lattice oxygen (O^{2-}) in the wurtzite ZnO structure, while the peak at 531.68 eV corresponds to oxygen vacancies or defect-related oxygen species. The higher binding energy component at 532.48 eV is associated with surface hydroxyl groups or adsorbed molecular oxygen species.[48]

3.3. Morphology and elemental analysis with FESEM and TEM

The morphological analysis of the synthesized ZnO NPs was carried out using FESEM and TEM techniques. The FESEM

images (Fig. 5a and b) reveal that particles of ZnO possess an assorted morphology including irregularly shaped flakes (angular and medium sphericity), flat oval shapes, irregular polyhedron, and hexagonal platelet-like structures.[49] The particles appear faceted and compact with clear and sharp edges devoid of surface roughness, which is characteristic of ZnO structures formed *via* thermal decomposition of precursors.[50] The corresponding particle size histogram (Fig. 5c) was generated from FESEM images using ImageJ software (the protocol is detailed in our previous work[43]) based on FESEM images, shows a broad size distribution with an average particle size of 146 ± 89 nm. Despite some particles exceeding the nanoscale threshold of 100 nm, majority of them fall within the nanometer regime that justifies their classification as NPS. Moreover, individual crystallites observed in the FESEM images often appear fused, contributing to an apparently larger particle size due to agglomeration or sintering effects during calcination at 350 °C.

To further substantiate this, TEM analysis (Fig. 5d and e) was conducted, which offers better contrast and resolution for particle size estimation. The TEM images clearly show well-dispersed particles with quasi-spherical to slightly elongated shapes, significantly smaller in size compared to those observed in FESEM. The size distribution histogram based on TEM measurements (Fig. 5f) indicates an average particle size of 40 ± 27 nm, reaffirming the nanoparticulate nature of the sample. This discrepancy between FESEM and TEM-derived sizes can be attributed to the higher resolution of TEM and its ability to resolve individual particles even within agglomerates. Thus, despite the larger apparent size from FESEM, the particles are correctly described as NPs based on the true primary particle size observed under TEM. The selected area electron diffraction (SAED) pattern (Fig. 5g) presents a series of concentric diffraction rings, which confirms the polycrystalline nature of the ZnO NPs. The well-defined diffraction rings indicate that the NPs exhibit good crystallinity, consistent with the thermal decomposition route used for synthesis.[51,52] The smaller size observed by TEM compared to FESEM might be due to the agglomeration of particles during calcination and the limitations of FESEM in resolving closely packed nanoparticles. Before TEM imaging, the samples were ultrasonicated in ethanol before drop-casting, which promoted dispersion and enabled measurements of individual crystallites.

Elemental composition analysis was carried out by using EDX, coupled with both TEM and FESEM techniques. The EDX spectrum obtained from the TEM (Fig. 5h) indicates the presence of Zn (45.27 atom%), O (35.45 atom%), C (3.53 atom%), and Cu (15.32 atom%). The Cu signal is likely due to the copper

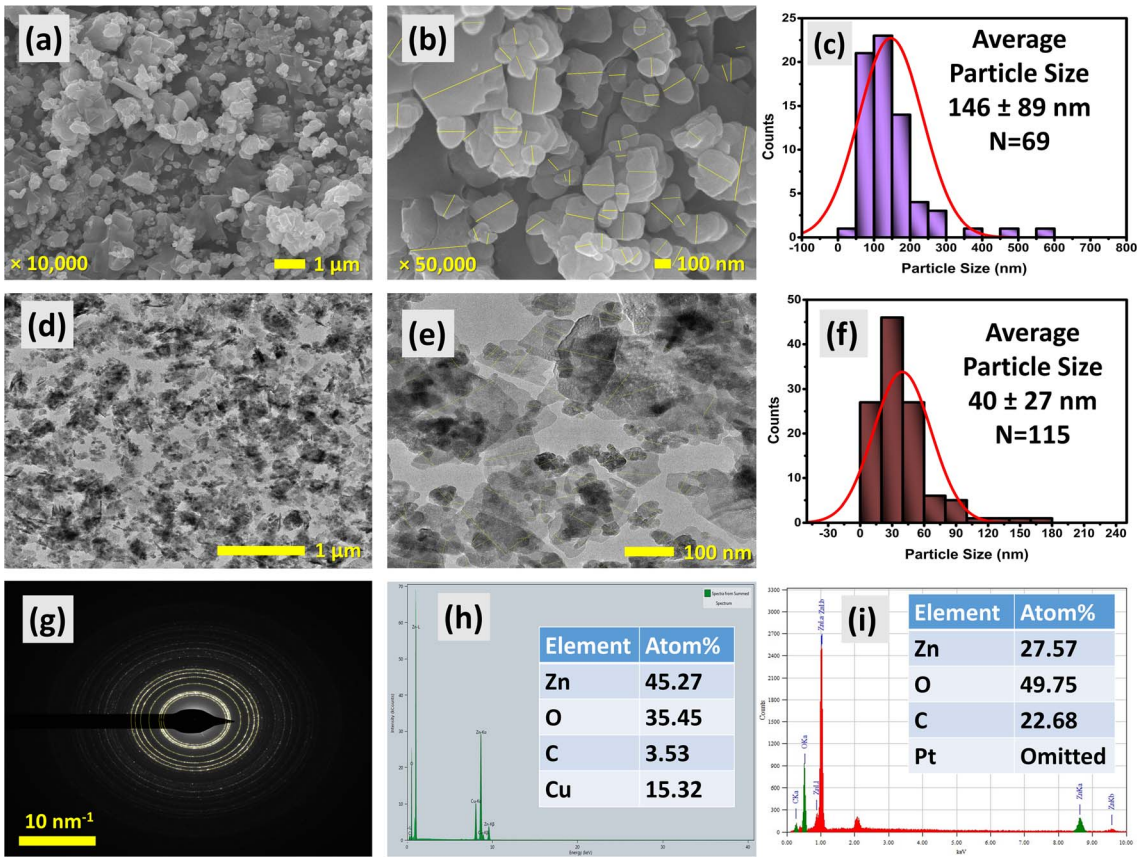

Fig. 5 (a and b) FESEM images, (c) particle size distribution histogram based on FESEM image, (d and e) TEM images, (f) particle size distribution histogram based on TEM image, (g) SAED pattern, (h) EDX spectrum and elemental composition based on TEM and (i) EDX spectrum and elemental composition based on FESEM. ImageJ software was used for particle and SAED ring size measurements.

TEM grid used for sample support, while the small C content may be attributed to residual surface carbon species or contamination. The EDX data from FESEM (Fig. 5i) also confirms the presence of Zn (27.57 atom%), O (49.75 atom%), and C (22.68 atom%). The higher carbon content in the FESEM-EDX may result from carbon tape used for sample mounting and environmental hydrocarbon contamination. Particularly, difference in atomic percentages between the two techniques may have resulted due to the differences in sampling volume, resolution, and instrument sensitivity. While TEM-EDX probes a thinner, localized region with greater sensitivity to light elements, FESEM-EDX captures a bulkier surface region, potentially leading to compositional averaging and higher background interference.

3.4. FTIR analysis

The FTIR spectrum of the synthesized ZnO NPs displays (Fig. 6a) distinct absorption bands that provide insight into the functional groups present on the NP surface. The slightly broad absorption band at 3495 cm^{-1} can be attributed to the stretching vibrations of –OH group, which is an indication of adsorbed moisture on ZnO surface.[53] NPs with high surface area typically show affinity towards water molecules to be adsorbed onto their surface. The peak at 1041 cm^{-1} may arise from residual surface-bound hydroxyl species or trace carbonate groups formed *via* atmospheric CO_2 adsorption during sample preparation. The band at 902 cm^{-1} is likely associated with bending vibrations of Zn–O or possibly out-of-plane C–H deformation from organic remnants.[54] Prominent peaks observed at 719 and 547 cm^{-1} are characteristic of Zn–O stretching vibrations, which confirm the formation of ZnO with a wurtzite crystal structure. These absorption bands are widely reported as fingerprints for Zn–O bonds in ZnO nanostructures and typically appear in the range from 400 to 600 cm^{-1}.[55] The peak at 547 cm^{-1} in particular is strongly characteristic for the Zn–O stretching mode, corroborating the successful synthesis and purity of ZnO NPs.[56] Additionally, the band near 719 cm^{-1} may indicate lattice vibrations involving oxygen and zinc atoms, supporting the presence of well-crystallized ZnO NPs.[57]

3.5. Raman analysis

The Raman spectrum of the synthesized ZnO NPs exhibits several distinct peaks that are consistent with the hexagonal wurtzite crystal structure of ZnO (Fig. 6b). The sharp band observed at 440 cm^{-1} corresponds to the E_2 (high) phonon mode, which is a characteristic vibrational feature of crystalline ZnO and is associated with the oxygen atom sublattice in the wurtzite lattice.[58] The prominent peak at 102 cm^{-1} is assigned to the E_2 (low) mode, which relates to the vibration of the zinc sublattice.[59] A strong band at 1071 cm^{-1} may be attributed to a multi-phonon scattering process or second-order Raman scattering, often observed in ZnO nanostructures due to resonance effects. The bands at 187 cm^{-1} and 725 cm^{-1} are indicative of defect-related or surface phonon modes, which commonly arise from oxygen vacancies, zinc interstitials, or other structural defects introduced during synthesis, especially in NPs derived from recycled or chemically treated sources.[60]

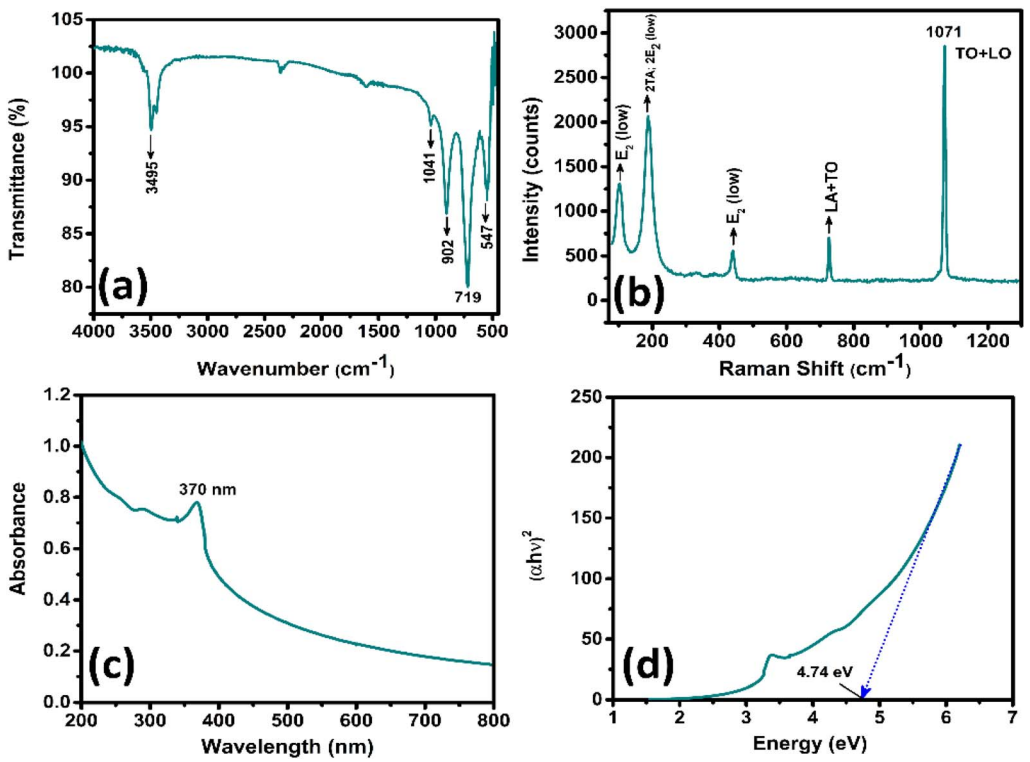

Fig. 6 (a) FTIR, (b) Raman and (c) UV-visible spectrum, and (d) normalized photon energy *vs.* $(\alpha h\nu)^2$ plot (Tauc plot) for band gap calculation of the synthesized ZnO NPs.

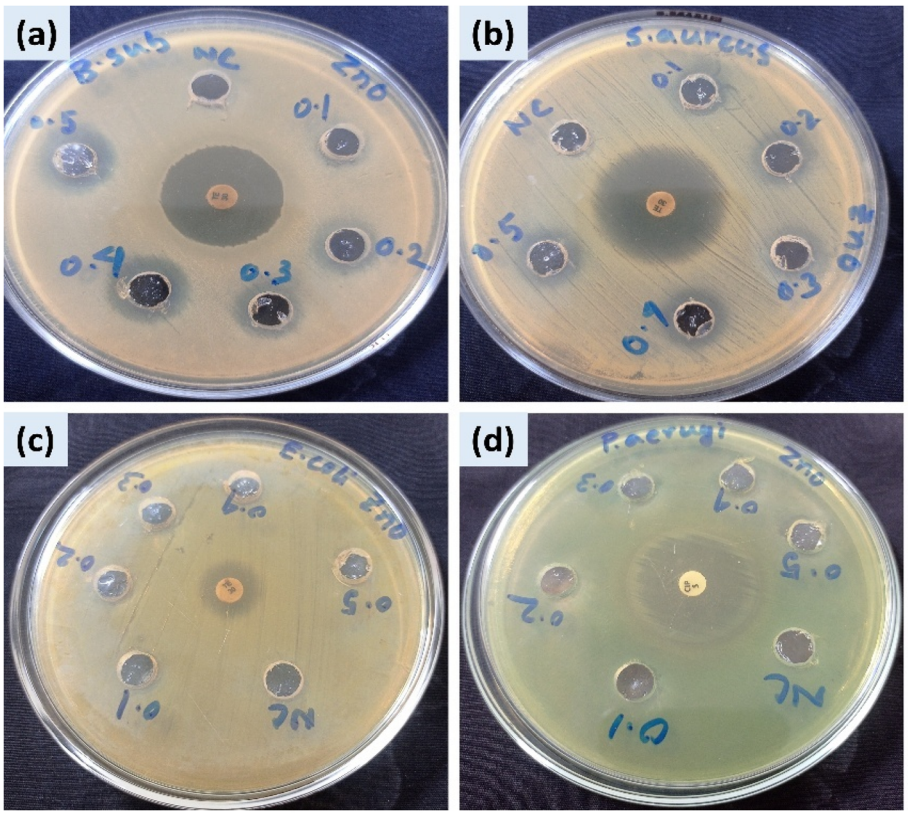

Fig. 7 Assessment of antibacterial activity of ZnO NPs against (a) *Bacillus subtilis* (b) *Staphylococcus aureus,* (c) *Escherichia coli* and (d) *Pseudomonas aeruginosa*.

3.6. Optical property analysis

The optical properties of the synthesized ZnO NPs were investigated using UV-Vis spectroscopy in the range of 200–800 nm. As shown in Fig. 6c, a strong absorption peak is observed at 370 nm, which is characteristic of the intrinsic band-to-band transition of ZnO and is consistent with the reported values for nanoscale ZnO materials.[61–64] This absorption behavior confirms the semiconductor nature of ZnO and suggests the presence of nanoscale crystallites, as the absorption edge tends to shift slightly due to quantum confinement effects in nanoparticles.[65] The optical band gap energy (E_g) of the synthesized ZnO NPs was determined by using the Tauc plot method, as presented in the following equation.[66]

$$\alpha h\nu = A(h\nu - E_g)^n \quad (28)$$

Here, α = absorption coefficient, $h\nu$ = photon energy, A = constant, and n = exponent that depends on the nature of the electronic transition. For ZnO, which exhibits a direct allowed transition, the value of n is taken as 2.[67] The Tauc plot (Fig. 6d), obtained by plotting $(\alpha h\nu)^2$ *versus* $h\nu$, reveals a linear region whose extrapolation to the energy axis gives the optical band gap. The optical band gap of the synthesized ZnO NPs was determined to be 4.74 eV from the Tauc plot analysis (Fig. 6d), a value significantly larger than that of bulk ZnO (~3.37 eV).[28] This substantial blue shift is primarily attributed to the quantum confinement effect which is characteristic of nanoscale materials. However, the magnitude of this shift is exceptionally large for the observed average particle size of ~40 nm. Therefore, it is likely that other factors are contributing to this value. The Tauc plot method is highly sensitive to the selected linear region for extrapolation, and an extrapolation from the steep, high-energy portion of the absorption spectrum may result in an overestimation of the band gap. Furthermore, microstrain within the crystal lattice, which was inferred from XRD analysis, and the presence of surface defects inherent to the wet chemical synthesis route can also alter the electronic band structure, contributing to the observed widening of the band gap.[68,69]

3.7. Antibacterial activity study

The antibacterial activity of the synthesized ZnO NPs against both Gram-positive and Gram-negative bacteria is shown in Fig. 7. The results (Table 6) indicate that the ZnO NPs exhibited a concentration-dependent inhibitory effect against the Gram-positive strains, with the zone of inhibition (ZOI) increasing from 1.1 ± 0.21 cm to 1.5 ± 0.55 cm for *S. aureus* and from 0.9 ± 0.21 cm to 1.7 ± 0.16 cm for *B. subtilis* as the concentration was raised from 0.2 to 0.5 mg mL^{-1}. For comparison, earlier studies on chemically synthesized ZnO NPs were considered that reported varying antibacterial activity depending on concentration. Against *S. aureus*, inhibition zones were observed in the

Table 6 Evaluation of antibacterial activity of battery waste-utilized ZnO NPs by agar well diffusion assay[a]

Zone of inhibition in cm					
		Gram positive bacteria		Gram negative bacteria	
Samples	Concentration	*S. aureus* ATCC 29737	*B. subtilis* ATCC 6633	*E. coli* ATCC 11229	*P. aeruginosa* ATCC 10145
ZnO	0.1 mg mL^{-1}	—	—	—	—
	0.2 mg mL^{-1}	1.1 ± 0.21	0.9 ± 0.21	—	—
	0.3 mg mL^{-1}	1.2 ± 0.16	1.2 ± 0.23	—	—
	0.4 mg mL^{-1}	1.3 ± 0.52	1.5 ± 0.19	—	—
	0.5 mg mL^{-1}	1.5 ± 0.55	1.7 ± 0.16	—	—
Positive control	30 and 5 μg disc of tetracycline (TE) and ciprofloxacin (CIP) respectively	3.3 ± 0.15 (TE)	3.1 ± 0.15 (TE)	2.2 ± 0.53 (TE)	2.9 ± 0.17 (CIP)
Negative control	—	—	—	—	—

[a] Tetracycline and ciprofloxacin disc was used as positive control and DMSO solvent as negative control.

range of 1.4 to 2.4 cm, with specific reports noting 2.4 ± 0.035 cm at 4 mg mL^{-1},[70] 1.76 ± 0.26 cm at 25–50 μg mL^{-1},[71] 1.4 cm at 10–20 μg mL^{-1},[72] 2.3 cm at 0.5 mg mL^{-1},[73] and 1.8 cm at 50 μg mL^{-1}.[74] In the case of *B. subtilis*, reported zones of inhibition include 0.9 cm at 50 μg mL^{-1},[75] 2.3 cm at 30 mg mL^{-1},[76] and 1.6 ± 0.17 cm at 0.5 mg mL^{-1}.[77]

In contrast, no significant inhibition was observed against the Gram-negative strains at our tested concentration. The positive controls (tetracycline and ciprofloxacin) displayed significantly larger ZOIs for all strains, while the negative control (DMSO) showed no inhibition.

These findings are consistent with previous studies where ZnO NPs exhibited stronger antibacterial activity against Gram-positive bacteria compared to Gram-negative strain.[78–80] The greater resistance of Gram-negative bacteria is attributed to their outer membrane containing lipopolysaccharides, which act as an additional barrier, limiting nanoparticle penetration and reactive oxygen species (ROS) interactions. Conversely, Gram-positive bacteria have a thicker peptidoglycan layer but lack this protective outer membrane, making them more susceptible to ZnO-induced damage.[81]

The antibacterial mechanism of ZnO NPs is multifaceted and has been widely reported in the literature. Firstly, ZnO NPs can adhere to bacterial cell walls, leading to physical disruption and increased membrane permeability. Secondly, under physiological conditions, ZnO can generate ROS such as hydrogen peroxide (H_2O_2), hydroxyl radicals ($^{\bullet}OH$), and superoxide anions ($O_2^{\bullet-}$), which cause oxidative stress and damage to cellular components including lipids, proteins, and DNA. Thirdly, the dissolution of Zn^{2+} ions from ZnO contributes to the disruption of bacterial enzymatic systems and metabolic pathways. Finally, NPs can penetrate cells, interfering with intracellular processes and ultimately leading to cell death.[81–83]

4 Conclusion

This research successfully demonstrates a simple, cost-effective, and environmentally benign method for synthesizing crystalline ZnO NPs from a hazardous waste source: the zinc shells of spent dry cell batteries. The synthesis, involving acid digestion and subsequent calcination at a relatively low temperature of 350 °C, proved effective in converting waste zinc into a high-value nanomaterial. The comprehensive characterization confirmed the formation of phase-pure ZnO with a hexagonal wurtzite crystal structure. An extensive crystallographic analysis using ten distinct models provided a reliable average crystallite size in the range of 32–40 nm, with the Halder–Wagner and size–strain plot methods showing the best fit to the experimental data. Morphological analysis by TEM confirmed this nanoscale dimension. Crucially, the waste-derived ZnO NPs exhibited significant antibacterial activity, showing a clear dose-dependent inhibitory effect against the Gram-positive bacteria *B. subtilis* and *S. aureus*. The lack of activity against Gram-negative bacteria suggests a selective mechanism of action, highlighting the importance of bacterial cell wall structure in determining susceptibility. This study not only presents a viable route for the valorization of toxic battery waste but also validates the potential of the resulting ZnO NPs as effective antibacterial agents for applications where targeting Gram-positive pathogens is desired.

Author contributions

Mashrafi Bin Mobarak: conceptualization, methodology, resources, funding acquisition, project administration, formal analysis, investigation, data curation, writing – original draft, writing – review & editing. Md Sohag Hossain: methodology, investigation, data curation. Fariha Chowdhury: formal analysis, investigation, data curation, writing – review & editing. Nourin Tarannum: methodology, investigation, data curation. Monira Binte Mesbah: formal analysis. Nazmul Islam Tanvir: formal analysis. Umme Sarmeen Akhtar: formal analysis. Samina Ahmed: supervision, resources.

Conflicts of interest

There is no conflict to declare.

Data availability

All data supporting the findings of this study are included in the main manuscript. Raw data are available from the corresponding author upon reasonable request.

Acknowledgements

This work was supported by the Bangladesh Council of Scientific and Industrial Research (BCSIR) under R&D project reference no. 39.02.0000.011.14.169.2023/877, dated: 17/09/2023. To improve the readability and overall presentation of the manuscript, the authors used ChatGPT as a writing assistant. They confirm that all content produced with AI support was carefully reviewed and revised, and they take full accountability for the accuracy and integrity of the final version.

References

1 Y. Liang, C.-Z. Zhao, H. Yuan, Y. Chen, W. Zhang, J.-Q. Huang, D. Yu, Y. Liu, M.-M. Titirici, Y.-L. Chueh, H. Yu and Q. Zhang, *InfoMat*, 2019, **1**, 6–32.
2 Zinc Carbon Battery Market Size & Forecast, **https://www.verifiedmarketresearch.com/product/zinc-carbon-battery-market/**, (accessed July 29, 2025).
3 P. Amaro and F. Santos, in *Encyclopedia of Electrical and Electronic Power Engineering*, ed. J. García, Elsevier, Oxford, 2023, pp. 130–140.
4 M. A. Hasan, R. Hossain and V. Sahajwalla, *J. Environ. Manage.*, 2024, **356**, 120461.
5 R. Farzana, R. Rajarao, P. R. Behera, K. Hassan and V. Sahajwalla, *Nanomaterials*, 2018, **8**, 717.
6 K. Lock and C. R. Janssen, *Environ. Pollut.*, 2005, **136**, 275–281.
7 M. Abdel-Tawwab, G. O. El-Sayed and S. H. Shady, *Int. Aquat. Res.*, 2016, **8**, 197–206.
8 L. M. Plum, L. Rink and H. Haase, *Int. J. Environ. Res. Public Health*, 2010, **7**, 1342–1365.
9 H. Schoofs, J. Schmit and L. Rink, *Molecules*, 2024, **29**, 3130.
10 B. Ebin, M. Petranikova, B.-M. Steenari and C. Ekberg, *Waste Manage.*, 2016, **51**, 157–167.
11 S. Malik, K. Muhammad and Y. Waheed, *Molecules*, 2023, **28**, 661.
12 M. B. Mobarak, M. F. Sikder, K. S. Muntaha, S. Islam, S. F. Rabbi and F. Chowdhury, *Nanoscale Adv.*, 2025, **7**, 2418–2445.
13 Z. Jiang, B. Liu, L. Yu, Y. Tong, M. Yan, R. Zhang, W. Han, Y. Hao, L. Shangguan, S. Zhang and W. Li, *J. Alloys Compd.*, 2023, **956**, 170316.
14 S. Raha and M. Ahmaruzzaman, *Nanoscale Adv.*, 2022, **4**, 1868–1925.
15 H. Samadi, R. Zarei Mohgadam and M. Gholipour Shahraki, *Mater. Chem. Phys.*, 2025, **345**, 131161.
16 V. R. Lebaka, P. Ravi, M. C. Reddy, C. Thummala and T. K. Mandal, *Nanomaterials*, 2025, **15**, 754.
17 M. H. Khan and A. S. W. Kurny, *J. Miner. Mater. Charact. Eng.*, 2012, **11**, 641–651.
18 M. Sohag Hossain, S. Alam Aumi, N. Tarannum, F. Chowdhury, M. S. Hossain, M. Farid Ahmed, N. Islam Tanvir, U. Sarmeen Akhtar, S. Ahmed and M. Bin Mobarak, *RSC Adv.*, 2025, **15**, 30564–30575.
19 T. Saha, M. B. Mobarak, M. N. Uddin, M. S. Quddus, M. R. Naim and N. S. Pinky, *Mater. Chem. Phys.*, 2023, 127979.
20 L. Ruilin, K. Y. Yee, N. A. Salleh, B. Deghfel, Z. Zakaria, M. K. Yaakob, H. R. Ong, W. Rahiman, H. Akbulut, D. Wang, S. Kheawhom and A. A. Mohamad, *Inorg. Chem. Commun.*, 2024, **170**, 113311.
21 O. García-Martínez, R. M. Rojas, E. Vila and J. L. M. de Vidales, *Solid State Ionics*, 1993, **63–65**, 442–449.
22 A. G. Joshi, S. Sahai, N. Gandhi, Y. G. R. Krishna and D. Haranath, *Appl. Phys. Lett.*, 2010, **96**, 123102.
23 B. B. Salem, G. Essalah, S. B. Ameur, B. Duponchel, H. Guermazi, S. Guermazi and G. Leroy, *RSC Adv.*, 2023, **13**, 6287–6303.
24 C. R. Mendes, G. Dilarri, C. F. Forsan, V. de, M. R. Sapata, P. R. M. Lopes, P. B. de Moraes, R. N. Montagnolli, H. Ferreira and E. D. Bidoia, *Sci. Rep.*, 2022, **12**, 2658.
25 Y. Shaban and N. A. Alharbi, *Environ. Sci. Pollut. Res.*, 2022, **29**, 47818–47831.
26 V. N. Kalpana, B. A. S. Kataru, N. Sravani, T. Vigneshwari, A. Panneerselvam and V. Devi Rajeswari, *OpenNano*, 2018, **3**, 48–55.
27 B. Bulcha, J. Leta Tesfaye, D. Anatol, R. Shanmugam, L. P. Dwarampudi, N. Nagaprasad, V. L. N. Bhargavi and R. Krishnaraj, *J. Nanomater.*, 2021, **2021**, 8617290.
28 M. Nabil, I. V. Perez-Quintana, M. Acosta, J. A. Mendez-Gamboa and R. Castro-Rodriguez, *Adv. Mater. Sci. Eng.*, 2021, **2021**, 9926544.
29 M. B. Mobarak, F. Chowdhury and S. Ahmed, *RSC Adv.*, 2024, **14**, 39874–39889.
30 M. Sharma, R. Nagar, V. K. Meena and S. Singh, *RSC Adv.*, 2019, **9**, 11170–11178.
31 M. Bhagwat, P. Shah and V. Ramaswamy, *Mater. Lett.*, 2003, **57**, 1604–1611.
32 K. C. Vinoth Kumar, T. Jani Subha, K. G. Ahila, B. Ravindran, S. W. Chang, A. H. Mahmoud, O. B. Mohammed and M. A. Rathi, *Saudi J. Biol. Sci.*, 2021, **28**, 840–846.
33 C. Stegmann, F. Muench, M. Rauber, M. Hottes, J. Brötz, U. Kunz, S. Lauterbach, H.-J. Kleebe and W. Ensinger, *RSC Adv.*, 2014, **4**, 4804–4810.
34 K. H. Kim and J. S. Chun, *Thin Solid Films*, 1986, **141**, 287–295.
35 M. B. Mobarak, S. Tabassum, M. S. Hossain, N. Tarannum, F. Chowdhury, M. S. Hossain, N. I. Tanvir and S. Ahmed, *RSC Adv.*, 2025, **15**, 35617–35633.
36 M. Hossain, M. Mahmud, M. B. Mobarak, S. Sultana, M. Shaikh, A. Ali and S. Ahmed, *Chem. Pap.*, 2022, **76**(11), 7245–7251.
37 P. Scherrer, *Nachr. Ges. Wiss. Goettingen, Math.-Phys. Kl.*, 1918, **2**, 8–100.
38 M. Hossain, M. Mahmud, M. B. Mobarak and S. Ahmed, *Chem. Pap.*, 2022, **76**, 1593–1605.

39 M. Rabiei, A. Palevicius, A. Monshi, S. Nasiri, A. Vilkauskas and G. Janusas, *Nanomaterials*, 2020, **10**, 1627.
40 A. Monshi, M. R. Foroughi and M. R. Monshi, *World J. Nano Sci. Eng.*, 2012, **2**, 154–160.
41 M. S. Hossain, M. M. Hasan, M. Mahmud, M. B. Mobarak and S. Ahmed, *Chem. Pap.*, 2023, **77**, 463–471.
42 H. Morkoç and Ü. Özgür, *Zinc Oxide: Fundamentals, Materials and Device Technology*, John Wiley & Sons, 2008.
43 M. Bin Mobarak, Md. S. Hossain, F. Chowdhury and S. Ahmed, *Arabian J. Chem.*, 2022, **15**, 104117.
44 M. S. Hossain, M. S. Hossain, S. Ahmed and M. B. Mobarak, *RSC Adv.*, 2024, **14**, 38560–38577.
45 M. B. Mobarak, S. A. Fahim, M. S. Hossain, F. Chowdhury, N. I. Tanvir, U. S. Akhtar and S. Ahmed, *ACS Sustainable Resour. Manage.*, 2025, **2**, 1528–1539.
46 J. Wu, Y. Fang, D. Zhang, S. Zhang, J. Wan, R. Wen, X. Zhou, N. Fu and Y. Lin, *J. Mater. Chem. A*, 2021, **9**, 14877–14887.
47 M. M. Alam, A. M. Asiri, M. T. Uddin, M. A. Islam and M. M. Rahman, *RSC Adv.*, 2018, **8**, 12562–12572.
48 M. Claros, M. Setka, Y. P. Jimenez and S. Vallejos, *Nanomaterials*, 2020, **10**, 471.
49 K. S. Shah, M. H. bin M. Hashim, M. Z. Emad, K. S. bin Ariffin, M. Junaid and N. M. Khan, *Arabian J. Geosci.*, 2020, **13**, 708.
50 V. Preethi, S. Anila Raj, V. G. Viju Kumar and V. G. Vidya, *Ionics*, 2025, **31**, 2997–3020.
51 R.-O. Moussodia, L. Balan, C. Merlin, C. Mustin and R. Schneider, *J. Mater. Chem.*, 2010, **20**, 1147–1155.
52 A. Dumbrava, D. Berger, G. Prodan, M. Badea, R. Olar, F. Moscalu and A. Diacon, *Appl. Phys. A*, 2018, **124**, 819.
53 K. Faaiza Naaz, A. Tiwari, A. H. Shaik, P. Indumathi, B. Brianna, A. Anwar and M. R. Chandan, *Green Chem. Lett. Rev.*, 2025, **18**, 2453532.
54 S. Mahalakshmi, N. Hema and P. P. Vijaya, *J. Bionanosci.*, 2020, **10**, 112–121.
55 P. Ramesh, K. Saravanan, P. Manogar, J. Johnson, E. Vinoth and M. Mayakannan, *Sens. Bio-Sens. Res.*, 2021, **31**, 100399.
56 T. Ahmad, V. Pandey, M. Saddam Husain, A. Adiba and S. Munjal, *Mater. Today: Proc.*, 2022, **49**, 1694–1697.
57 S. Rafique, A. K. Kasi, J. K. Kasi, Aminullah, M. Bokhari and Z. Shakoor, *Nanomater. Nanotechnol.*, 2020, **10**, 1847980419895741.
58 Z. Peng, G. Dai, W. Zhou, P. Chen, Q. Wan, Q. Zhang and B. Zou, *Appl. Surf. Sci.*, 2010, **256**, 6814–6818.
59 I. Musa, N. Qamhieh and S. T. Mahmoud, *Results Phys.*, 2017, **7**, 3552–3556.
60 R. Cuscó, E. Alarcón-Lladó, J. Ibáñez, L. Artús, J. Jiménez, B. Wang and M. J. Callahan, *Phys. Rev. B:Condens. Matter Mater. Phys.*, 2007, **75**, 165202.
61 H. Udayagiri, S. S. Sana, L. K. Dogiparthi, R. Vadde, R. S. Varma, J. R. Koduru, G. S. Ghodake, A. R. Somala, V. K. N. Boya, S.-C. Kim and R. R. Karri, *Sci. Rep.*, 2024, **14**, 19714.
62 F. Rahman, M. A. Majed Patwary, Md. A. Bakar Siddique, M. S. Bashar, Md. A. Haque, B. Akter, R. Rashid, Md. A. Haque and A. K. M. Royhan Uddin, *R. Soc. Open Sci.*, 2022, **9**, 220858.
63 B. A. Al-Mur, *Water*, 2023, **15**, 455.
64 S. Saeed, S. Nawaz, A. Nisar, T. Mehmood, M. Tayyab, M. Nawaz, S. Firyal, M. Bilal, A. Mohyuddin and A. Ullah, *Mater. Res. Express*, 2021, **8**, 035004.
65 S. Mandal, R. K. Singha, A. Dhar and S. K. Ray, *Mater. Res. Bull.*, 2008, **43**, 244–250.
66 F. Chowdhury, M. B. Mobarak, M. Hakim, M. N. Uddin, M. S. Hossain, U. S. Akhter, D. Islam, S. Ahmed and H. Das, *New J. Chem.*, 2024, **48**, 17038–17051.
67 A. A. Mohamad, M. S. Hassan, M. K. Yaakob, M. F. M. Taib, F. W. Badrudin, O. H. Hassan and M. Z. A. Yahya, *J. King Saud Univ., Eng. Sci.*, 2017, **29**, 278–283.
68 P. K. Samanta, *Ann. Univ. Craiova, Phys.*, 2018, **28**, 17–23.
69 M. Ahmar Rauf, M. Owais, R. Rajpoot, F. Ahmad, N. Khan and S. Zubair, *RSC Adv.*, 2017, **7**, 36361–36373.
70 M. D, K. P and V. R. Kolli, *Int. J. Appl. Pharm.*, 2018, 224–228.
71 R. M. Al-Mosawi, H. A. Jasim, A. Haddad, R. M. Al-Mosawi, H. A. Jasim and A. Haddad, *AIMS Microbiol.*, 2023, **9**, 90–107.
72 P. P. Mahamuni, P. M. Patil, M. J. Dhanavade, M. V. Badiger, P. G. Shadija, A. C. Lokhande and R. A. Bohara, *Biochem. Biophys. Rep.*, 2019, **17**, 71–80.
73 M. F. Khan, M. Hameedullah, A. H. Ansari, E. Ahmad, M. B. Lohani, R. H. Khan, M. M. Alam, W. Khan, F. M. Husain and I. Ahmad, *Int. J. Nanomed.*, 2014, **9**, 853–864.
74 Q.-A. Naqvi, A. Kanwal, S. Qaseem, M. Naeem, S. R. Ali, M. Shaffique and M. Maqbool, *J. Biol. Phys.*, 2019, **45**, 147–159.
75 K. Nithya and S. Kalyanasundharam, *OpenNano*, 2019, **4**, 100024.
76 M. F. Elkady, H. Shokry Hassan, E. E. Hafez and A. Fouad, *Bioinorg. Chem. Appl.*, 2015, **2015**, 1–20.
77 M. F. Khan, A. H. Ansari, M. Hameedullah, E. Ahmad, F. M. Husain, Q. Zia, U. Baig, M. R. Zaheer, M. M. Alam, A. M. Khan, Z. A. AlOthman, I. Ahmad, G. M. Ashraf and G. Aliev, *Sci. Rep.*, 2016, **6**, 27689.
78 N. Babayevska, Ł. Przysiecka, I. Iatsunskyi, G. Nowaczyk, M. Jarek, E. Janiszewska and S. Jurga, *Sci. Rep.*, 2022, **12**, 8148.
79 Z. Emami-Karvani and P. Chehrazi, *Afr. J. Microbiol. Res.*, 2011, **5**, 1368–1373.
80 I. El-Habib, H. Maatouk, A. Lemarchand, S. Dine, A. Roynette, C. Mielcarek, M. Traoré and R. Azouani, *J. Funct. Biomater.*, 2024, **15**, 195.
81 B. Abebe, E. A. Zereffa, A. Tadesse and H. C. A. Murthy, *Nanoscale Res. Lett.*, 2020, **15**, 190.
82 S. Jiang, K. Lin and M. Cai, *Front. Chem.*, 2020, **8**, 580.
83 A. Sirelkhatim, S. Mahmud, A. Seeni, N. H. M. Kaus, L. C. Ann, S. K. M. Bakhori, H. Hasan and D. Mohamad, *Nano-Micro Lett.*, 2015, **7**, 219–242.